Journal of Alloys and Compounds 1047 (2025) 184918

Contents lists available at ScienceDirect

Journal of Alloys and Compounds

journal homepage: www.elsevier.com/locate/jalcom

Formation of single-phase crystalline and amorphous high-entropy ZrTiTaMoWNi thin films under near-equilibrium condensation conditions

Anna Kornyushchenko [a,b,*], Vyacheslav Perekrestov [b], Marilena Tomut [a,c], Harald Rösner [a], Martin Peterlechner [d], Gerhard Wilde [a,e]

[a] University of Münster, Institute of Materials Physics, Münster 48149, Germany
[b] Sumy State University, Laboratory of Vacuum Nanotechnologies, Sumy 40007, Ukraine
[c] GSI Helmholtz Center for Heavy Ion Research, Darmstadt 64291, Germany
[d] Karlsruhe Institute of Technology, Laboratory for Electron Microscopy, Karlsruhe 76131, Germany
[e] Herbert Gleiter International Institute, Liaoning Academy of Materials, Shenyang 110167, PR China

ARTICLE INFO

Keywords:
Single-phase crystalline high-entropy alloys
Amorphous high entropy alloys
Thin films
Radiation hardness
Near-equilibrium condensation

ABSTRACT

Using magnetron sputtering of a segmented target in high-purity argon, this study investigates how the formation mechanisms of Zr–Ti–Ta–Mo–W–Ni high-entropy thin films depend on process parameters such as sputtering power P_w, substrate temperature T_c, and Ni concentration. At Ni concentrations of 8–15 at% and low vapor supersaturation levels (P_w=15 W, T_c=280–500 °C), structurally stable and chemically uniform high-entropy amorphous coatings are formed. Transmission electron microscopy (TEM) investigations have shown that the crystallization of the amorphous coatings occurs in the form of a single bcc phase at an annealing temperature of 800°C. Furthermore, it has been shown that at $T_c = 440$°C, Pw = 15 W, and reduced Ni content (~3 at%), the bcc crystals preferentially nucleate and grow as nano-patterns aligned parallel to the (310) plane. Additionally, amorphous coatings demonstrate increased resistance to 4.8 MeV/u Au ion irradiation at a fluence of 5×10^{13} ions/cm^2, indicating their suitability as radiation-resistant protective layers.

1. Introduction

It is well known that the recently suggested concept of a high-entropy state is based on the mixing of five or more chemical elements in atomic fractions between 5 and 35 at% [1]. The configurational entropy of mixing is known to be proportional to the number of alloy constituents. Increased configurational entropy at elevated temperatures minimizes the Gibbs free energy, which in turn compensates for the formation enthalpy of intermetallic compounds and thereby favors the formation of single-phase solid solutions. The formation process of a solid solution that is chemically homogeneous at the atomic level is influenced by the physicochemical properties of the constituent elements. The latter include the difference in the atomic sizes of the constituent elements [1,2]. Thus, relatively small deviations from the average atomic size increase the probability of their mutual substitutional solubility and lead as a result to the formation of solid solution phases even at considerable solute concentrations. However, a significant difference in atomic sizes increases the probability for amorphous phase formation [1,2]. Besides that, parameters such as the electronegativity of the constituent elements, the contribution of entropy to the Gibbs free energy, and the total concentration of valence electrons [3,4] influence to different extents the phase formation process and thus impact the resulting phase state of any high-entropy alloy [1]. Undoubtedly, the degree of mutual intermixing (and solution formation) of the constituent elements of a high-entropy alloy also largely depends on the technological parameters applied during alloy synthesis.

A homogeneous composition distribution of the deposited HEA thin films can be achieved through atomic condensation of the corresponding stoichiometric vapor flows. In most cases, ion sputtering of alloyed or segmented targets is used to create equiatomic vapor flows [5,6]. Magnetron sputtering plays an important role among different ion sputtering preparation methods. This method allows the formation of films with controllable microstructure, chemical composition and surface morphology by adjusting deposition parameters. Depending on the technological process parameters, HEAs can be synthesized in the form of single-phase and multi-phase solid solution phases, amorphous phases, crystalline-amorphous dual phases [7], and in the form of nanostructures [8,9].

* Corresponding author at: University of Münster, Institute of Materials Physics, Münster 48149, Germany.
E-mail address: korniusg@uni-muenster.de (A. Kornyushchenko).

https://doi.org/10.1016/j.jallcom.2025.184918
Received 11 September 2025; Received in revised form 25 October 2025; Accepted 6 November 2025
Available online 12 November 2025

HEAs attract significant research interest due to their numerous unique physical property combinations that are often different from conventional metallic alloys. These include high strength [10,11], structural and temperature stability [12], catalytic properties [13,14], corrosion resistance [15,16], anti-oxidative properties [17] and outstanding tribological properties [18]. Of particular importance is the study of high-entropy systems based on refractory metals, which can become the basis of structural materials for nuclear power applications [19–21]. It is well known that to prevent the zirconium vapor reaction in nuclear reactors, protective coatings can be applied to the outer surface of the zirconium cladding of fuel elements. However, it is worth mentioning that the practical synthesis of nanocrystalline HEAs is a rather challenging technological task. Therefore, from scientific and applied points of view, it is important to establish the transition from the crystalline to an amorphous phase and establish the technological conditions that allow the formation of HEA 3D systems in the form of patterns consisting of individual weakly interconnected nanocrystals. As shown by previous studies on the preparation of condensates of individual metals, this transition is possible when the vapor (plasma) - condensate system approaches thermodynamic equilibrium [22].

Based on the above, the main goal of this work is to study the effect of approaching thermodynamic equilibrium in the plasma-condensate system during the formation of Zr–Ti–Ta–Mo–W–Ni thin films and to adjust the Ni concentration to enable the transition from the amorphous to the crystalline state of the corresponding high-entropy condensates. Due to their potential importance as radiation-shielding materials, their resistance to irradiation with high-energy Au ions was also investigated systematically.

2. Experimental

2.1. Sample preparation

A technique for formation of HEA layers has been used that is based on unbalanced direct current magnetron sputtering of a segmented target with the elemental constituents in high-purity argon under the action of plasma onto the growth surface. For the fabrication of the segmented target 99,99 % pure Zr, Ti, Ta, Mo, W, Ni metals have been utilized (Fig. 1). The layers have been deposited on KCl cleavages and glass substrates. The developed technological approach is based on the phase transition of sputtered substances into the condensed state under conditions close to thermodynamic equilibrium in plasma-condensate systems [22–25].

When studying the structure formation mechanisms of single-metal patterned nanosystems [22–25], we have found that the presence of even small amounts of chemically active residual gases during the condensation of weak vapor flows determines the violation of the spatially distributed growth selectivity of the individual nanocrystals and, as a result, leads to the formation of continuous, most probably amorphous films of oxides, nitrides, etc. Therefore, considerable attention has been devoted to the thorough purification of the working gas argon. For the purpose of controlled Ar purification, the vacuum chamber was equipped with two additional titanium (Ti) magnetron sputtering devices and with a MX7304A mass spectrometer. In this case, the purification procedure was based on the absorption of chemically active residual gases by the titanium film that acts as a strong residual gases getter. The resulting Ti layer has been deposited on the inner surface of the working chamber. The purification of the working gas continued throughout the deposition process of the high-entropy layers. The total partial pressure of chemically active gases at an argon pressure of $\sim$ 2.5 Pa was $\sim 8{\cdot}10^{-8}$ Pa. The schematical representation of the sputtering process is indicated in Fig. 1.

2.2. Realization of near-equilibrium conditions during the condensation of Zr–Ti–Ta–Mo–W–Ni layers

It is well known that the main technological parameters that affect the structure formation mechanism include the vapor pressure above the growth surface (P_c) and the corresponding equilibrium pressure value (P_e), as well as the growth surface temperature (T_c). Together, these parameters determine the relative supersaturation of the deposited vapors (ξ) in the form of the relationship [25]:

$$\xi \approx \frac{P_c - P_e}{P_e} \tag{1}$$

Conditions close to thermodynamic equilibrium in plasma-condensate systems can be described in terms of small values of the relative supersaturation ξ. At the same time, the equilibrium pressure value P_e depends on the desorption energy E_d of the adatoms and the growth temperature T_c according to the expression [22,25]:

$$P_e \propto \exp\left(-\frac{E_d}{k_b T_c}\right) \tag{2}$$

Here k_b is the Boltzmann constant.

It should be noted that in the presence of a significant number of components in the vapor flow, it is necessary to consider the partial

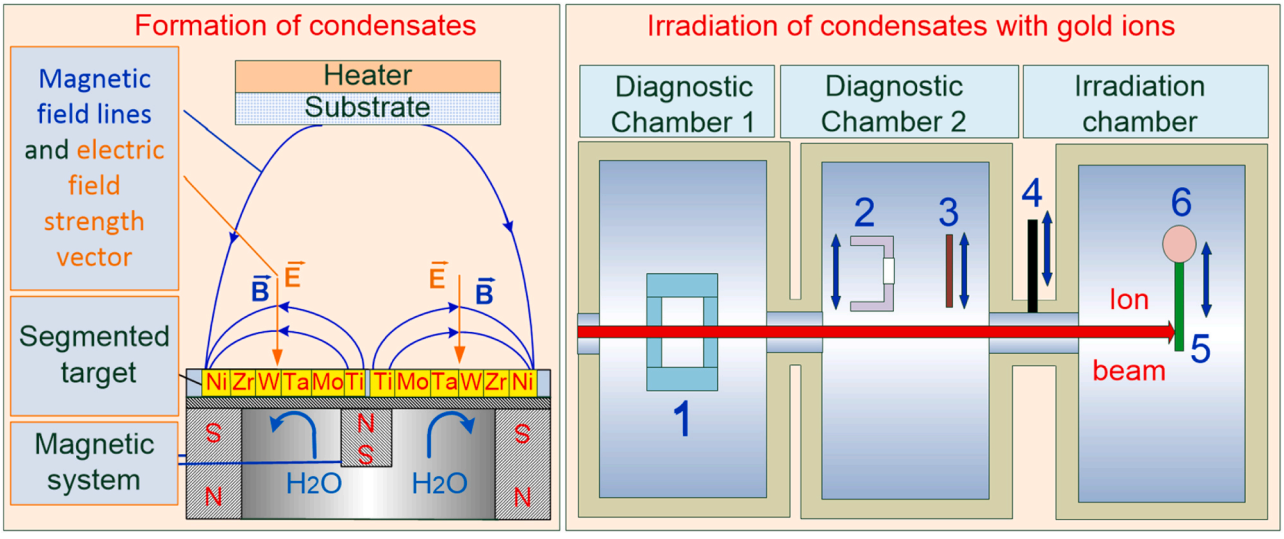

Fig. 1. Schematical representation of the sputtering process and the flow chart of the irradiation process (1 – the slits; 2 – Faraday cup; 3 – the luminescence screen 1; 4 – the gate valve; 5 – the luminescence screen 2; 6 – the samples holder).

pressure of each component and also to take into account the structure and elemental composition of the growth surface. All these factors significantly complicate the understanding and calculations of the numerical value of the relative supersaturation. At the same time, according to expressions (1) and (2) the transition from amorphous to crystalline phase state in the process of their formation is possible when the deposited flow of the multicomponent vapor (or P_c) is reduced by reducing the power P_w applied to the magnetron sputtering device, with a simultaneous increase in T_c. Because these two technological parameters are well controlled, it is not necessary to determine the precise numerical value of ξ. Additionally, it is preferable to use alloy components with approximately equal values of P_c at a fixed T_c. In the present study, for the Zr–Ti–Ta–Mo–W–Ni system, the above-mentioned criterion was taken into account during the selection of the constituent elements, with the exception of Ni. The refractory metals have been chosen in such a way that they have comparable and rather low values of equilibrium pressure at the same temperature. As a result, for the chemical elements selected for the coating composition, approaching of the plasma-condensate system conditions to the thermodynamic equilibrium can be performed while maintaining the nominal elemental composition of the deposited film.

When using only one external magnetic section in the magnetron sputtering, i.e., unbalanced magnetron sputtering, the magnetic field approaches directly to the substrate surface, which in turn significantly enhances the influence of the plasma onto the growth surface. As a result of such plasma effect, the growth surface temperature T_c increases. Besides that, the direct energy transfer from plasma particles to the adsorbed atoms takes place in this case. This plasma-induced effect reduces the probability of adatoms full thermal accommodation, thus facilitating their re-evaporation. In other words, the effect of the plasma onto the growth surface reduces the desorption energy to an effective value [22,25]:

$$E_{df} = E_d - \delta E \tag{3}$$

where δE is the stochastic value of the desorption energy decrease, which has an average value proportional to the plasma temperature.

2.3. Characterization

X-ray diffraction (XRD) analyses were conducted using a D5000 X-ray diffractometer (Siemens) with Cu K_α radiation. Measurements were performed in Bragg-Brentano geometry, utilizing a step size of 0.02° and an integration time of xy seconds while rotating the sample stage. The surface morphology and elemental composition of the high-entropy alloy (HEA) samples were examined via scanning electron microscopy (SEM, Nova NanoSEM 230 FEI), equipped with an energy-dispersive X-ray spectroscopy (EDX) detector (EDAX) for localized elemental analysis. The film thickness was measured using a BRUKER Dektak XT Profilometer.

Microstructural characterization was carried out using transmission electron microscopy (TEM, FEI Titan Themis 60–300 G3), which features a high-brightness field emission gun (XFEG), a monochromator, a C_s image corrector, and a quadrupole EDS system for sensitive chemical analysis. Additional detectors included a high-angle annular dark-field (HAADF) detector (Fischione Model 3000) and a 4k × 4k CMOS camera (Ceta). TEM analyses encompassed bright-field imaging, high-resolution TEM, selected area electron diffraction (SAED), and chemical composition mapping. The TEM was operated at an acceleration voltage of 300 kV and an extraction voltage of 3.45 kV. Scanning transmission electron microscopy (STEM) combined with HAADF imaging was employed to investigate the structural and compositional features of the HEA films.

For lamella preparation, a dual SEM/FIB system (ZEISS Crossbeam 340) was used. To minimize surface damage during FIB milling, a protective layer of platinum was deposited prior to lamella extraction. Post-irradiation swelling effects were assessed using a Keyence VK-X laser scanning microscope (LSM), providing precise topographical measurements of the sample surface.

2.4. Ion irradiation

Ion beam irradiation was performed at the linear accelerator UNILAC at GSI (Helmholtz-Zentrum für Schwerionenforschung Darmstadt) at the M3-Branch beamline. The irradiation experiments of this work have been performed in the oven chamber at 10^{-6}–10^{-7} mbar vacuum at room temperature. The HEAs have been irradiated with Au ions having energies 4.8 MeV/u to total fluences $1{\cdot}10^{11}$ ions/cm^2; $2{\cdot}10^{12}$ ions/cm^2; $5{\cdot}10^{12}$ ions/cm^2; and $5{\cdot}10^{13}$ ions/cm^2, respectively. The flow chart of the irradiation process is given in Fig. 1.

3. Results and discussion

3.1. Structural and morphological characteristics of Zr–Ti–Ta–Mo–W–Ni layers

The first series of experiments has been performed to obtain Zr–Ti–Ta–Mo–W–Ni films at relatively low (P_w=15 W, T_c=280°C) and high (P_w=85 W, T_c=60°C) supersaturations on fresh KCl single crystal cleavages. Fig. 2 shows the representative HR-TEM, SAED patterns, and BF STEM images of the HEAs layers. The HRTEM image (Fig. 2a and Fig. 2c) shows no crystalline areas. Diffuse halos typical for amorphous alloys are observed in the SAED patterns (Fig. 2b), that additionally confirm the amorphous nature of the structure investigated. The variations in contrast are attributed to variations in the thickness because of the increased surface roughness of the layers obtained at high supersaturations. A pronounced surface roughness (Fig. 2d) can be caused by insufficient energy of the depositing ions and, as a result, by their low mobility at increased supersaturation values ξ. This effect has been reported previously for magnetron sputtering [26]. The structural disordering of the obtained layer is also explained by random atom-by-atom adatom attachments on the growth surface that occur according to Poisson statistics with the possibility of realizing rather weak chemical bonds.

With a decrease in ξ by means of a decrease of the discharge power, and increase in the growth temperature, the layer structure becomes more homogeneous (Fig. 2e-h). No crystallites or ordered regions are detectable in the HR-TEM image (Fig. 2e) for layers grown at 280°C. Electron diffraction additionally confirms that the films are amorphous (Fig. 2f). However, the radial intensity distribution in the electron diffraction patterns is less blurred. These facts may indicate some structural ordering at the level of short-range order, that is additionally confirmed by azimuthal integral profiles (Fig. 3) obtained using PASAD electron diffraction analysis [27]. In contrast, a more homogeneous morphology (Fig. 2h) seems to arise from a higher diffusivity of the atomic species on the surface at higher growth surface temperatures under conditions of low supersaturation.

Based on the STEM-EDX results, layers with a uniform elemental distribution are formed both at relatively low supersaturation (Fig. 4a) and at higher supersaturation (Fig. 4b), with no observable signs of segregation. Under conditions of high supersaturation, layers with a composition of $Ti_{0.26}Ta_{0.17}Mo_{0.18}Ni_{0.17}$ $Zr_{0.13}W_{0.09}$ are obtained, the decrease in the ξ value determines the formation of $Ti_{0.28}Ta_{0.21}$ $Ni_{0.18}Mo_{0.11}Zr_{0.11}W_{0.11}$ layers. From the distribution of the elemental composition at relatively low (Fig. 4a) and high (Fig. 4b) supersaturations, we can conclude that the degree of mixing of the components decreases with the increase of the supersaturation of the depositing multicomponent vapor.

After annealing of the low-temperature formed films (structure in Fig. 2a-d) in vacuum for a prolonged period of time at a temperature of 280°C, a structural reorganization occurred at the short-range order level (Fig. 5). This is evidenced by the change in the radial intensity

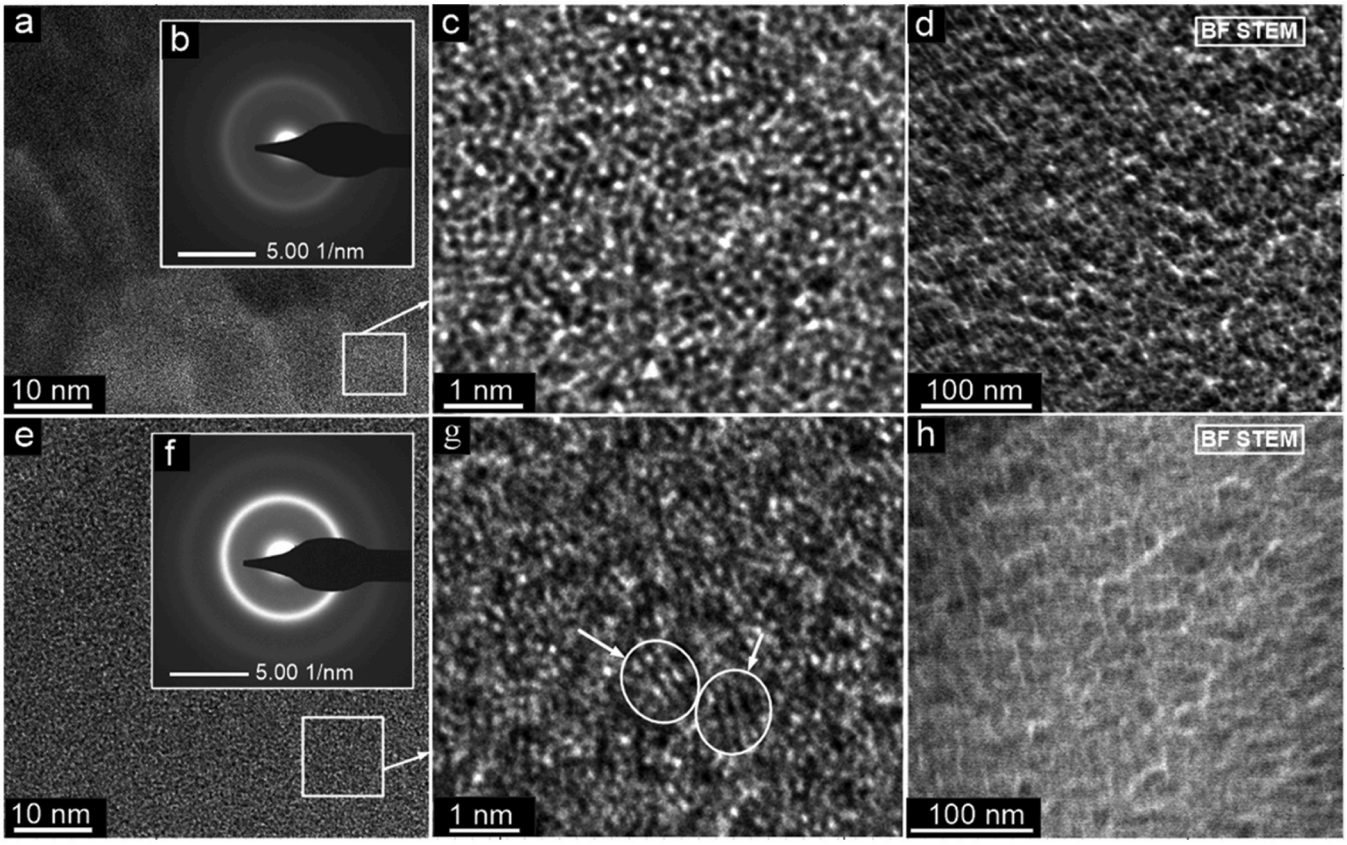

Fig. 2. Results of HRTEM studies at different magnifications, electron diffraction patterns as well as BF STEM images of ZrTiTaMoWNi layers obtained at $P_w = 85$ W, $T_c = 60°C$ (a,b,c,d) and formed at $P_w = 15$ W, $T_c = 280°C$ (e, f, g, h).

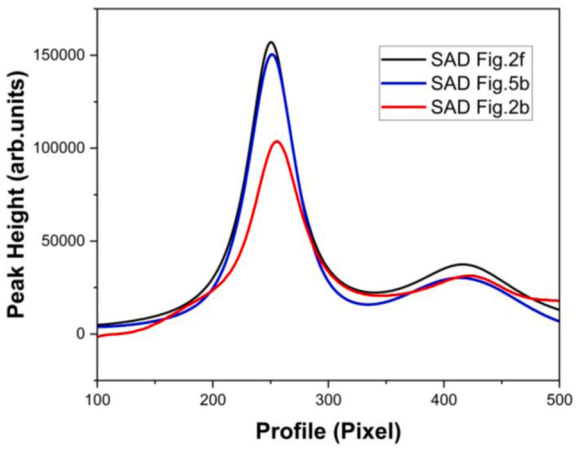

Fig. 3. Azimuthal integral profiles obtained from the electron diffraction patterns.

distribution of the electron diffraction patterns before (Fig. 2b) and after (Fig. 5b) annealing, as shown in the azimuthal integral profiles in Fig. 3. In addition, cracks appeared in the films after the annealing (Fig. 5c), which also indicates a restructuring. At the same time, annealing experiments with samples synthesized at $P_w = 15$ W, $T_c = 280°C$ have not shown any evidence of morphological or structural changes after their long-term annealing at 280°C. It is important to emphasize that under the technological parameters of the first series of experiments, the single-crystalline state of the KCl substrate does not promote the transition to a crystalline phase.

In the second series of experiments, the supersaturation was further reduced by increasing the growth surface temperature up to 400°C using the previous value of the magnetron sputtering power (P_w=15 W). The concentration of Ni in the films varied from 3 to 8 at% and glass was used as substrate material. Despite the sufficiently high T_c values and relatively small deposition vapor flows in the presence of an increased Ni concentration, according to X-ray phase studies, the layers were amorphous (Fig. 6a,b,c).

The surface investigations by SEM at different magnifications indicate the formation of layers with featureless morphologies and smooth surfaces (Fig. 6a,b). In this case, coating layers with a composition of $Ti_{0.25}Ta_{0.22}$ $Mo_{0.21}Zr_{0.12}W_{0.12}$ $Ni_{0.08}$ are formed with a uniform distribution of the chemical elements (Fig. 6d). The stability of the amorphous phase has been investigated through in-situ heating experiments inside the TEM. For this purpose, a TEM lamella with a protective Pt coating has been prepared. The initial distribution of the elementals before the heating indicates insignificant changes in the elemental composition along the thickness of the lamella and a high degree of intermixing of the components (Fig. 7a,b). The transition to the crystalline phase was recorded after annealing directly in the TEM at a temperature of 800°C. The crystallization process is observed in Fig. 6f, which indicates the presence of a bcc phase with a lattice constant of 0.321 nm. At the same time, the transition to the crystalline phase is accompanied by the diffusion of Pt atoms to a depth of ~1.3 μm and Ti atoms to the surface of the sample (Fig. 7d,e). The above-described processes were not observed at annealing temperatures below 800°C (Fig. 7c), which might be due to the typical Arrhenius-type temperature dependence of diffusional processes. Additionally, the migration of a transformation front, as involved in the crystallization of an amorphous phase, is known to accelerate the atomic mobility.

The transition to the crystalline phase was observed when the Ni concentration was reduced to 3 at%, as well as under the condition of

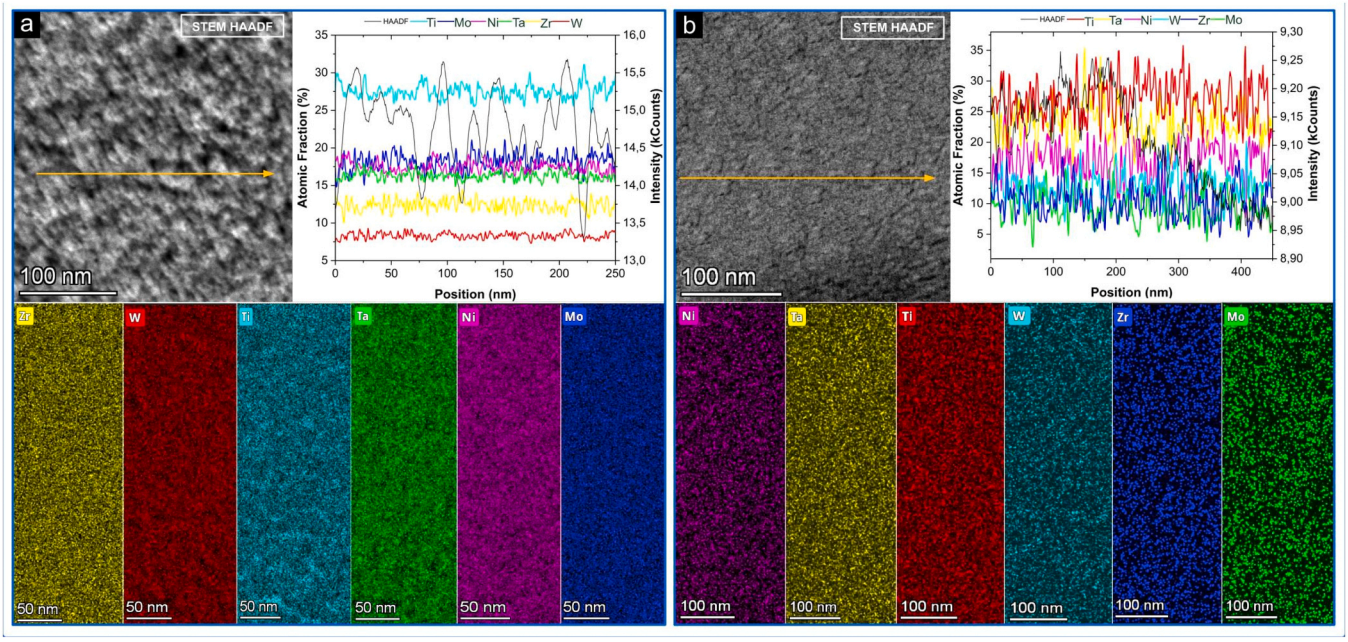

Fig. 4. Elemental analyses of the layers' using STEM-EDX.

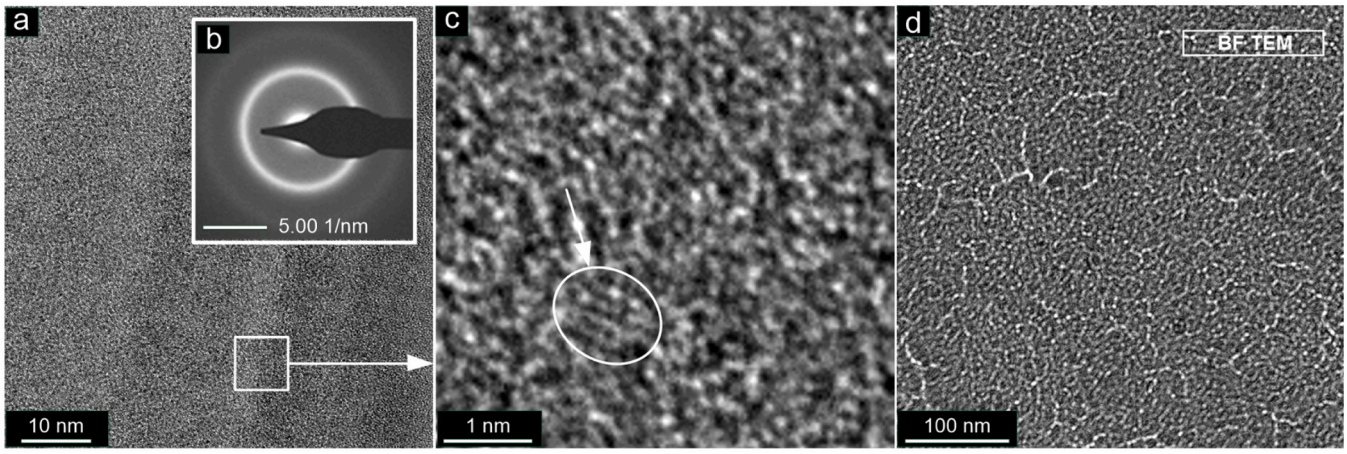

Fig. 5. Results of HR-TEM, SAED as well as BF-TEM of the layers annealed at 280°C.

the magnetron sputtering power remaining at (P_w=15 W) and the growth surface temperature increasing up to 440°C. The specified transition, in our case, is supposed to occur due to the decrease in relative supersaturation with an increase in T_c and a possible decrease in entropy due to a decrease in the nickel concentration. In this case, $Ti_{0.3}Ta_{0.21}Mo_{0.18}Zr_{0.15}W_{0.13}Ni_{0.03}$ layers were formed on glass, the concentration of the components is presented without the oxygen component. The transition to the crystalline phase itself was accompanied by the formation of a weakly interconnected system of crystals in the form of patterns (Fig. 8a-c). At the same time, SEM studies of the growth surface at increased resolution (Fig. 8c) indicate their atomically rough surface, which probably determines its chemical activity and the corresponding adsorption of a significant amount of oxygen on the surface (Fig. 8d). It should be noted, that SEM and EDX investigations have been performed in different substrate positions, and results obtained show homogeneity of the layer morphology and chemical composition. The films with such homogeneous morphology can be obtained on substrates with areas few cm^2.

TEM, HR-TEM, SAED, STEM HAADF investigations of the layer structures are presented in Fig. 9a-f. XRD studies (Fig. 9g) indicate the presence of only one diffraction maximum (Fig. 9g), which corresponds to an interplanar distance of 0.1026 nm. The limited information from X-ray diffraction studies due to the strong texture was supplemented by TEM (Fig. 9a) and HR-TEM investigations (Fig. 9b,c) and electron diffraction (SAED) (Fig. 9d). The analysis of the results indicates that the middle parts of the elongated structural elements have a structure close to a single-crystalline state. The conclusion is confirmed by HR-TEM investigations (Fig. 9c) and by the corresponding electron diffraction patterns (Fig. 9d). The distribution of the elemental compositions (Fig. 9h) along the layer thickness indicates its homogeneity, as well as the concentration of oxygen predominantly on the surface.

The evaluation of the electron diffraction patterns showed that layers are formed, based on a crystalline phase with bcc structure having a lattice constant of ~ 0.321 nm. However, as shown by STEM (Fig. 9e,f), structural fragments nucleate and grow over time on the surface of the central crystalline part, which have a predominant growth direction and represent the major volume fraction of the condensate. Based on this, it can be assumed that the side fragments cause the dominant contribution to the XRD signal and are similar in crystal structure to the central parts. It should also be emphasized that the distance between the (310) planes

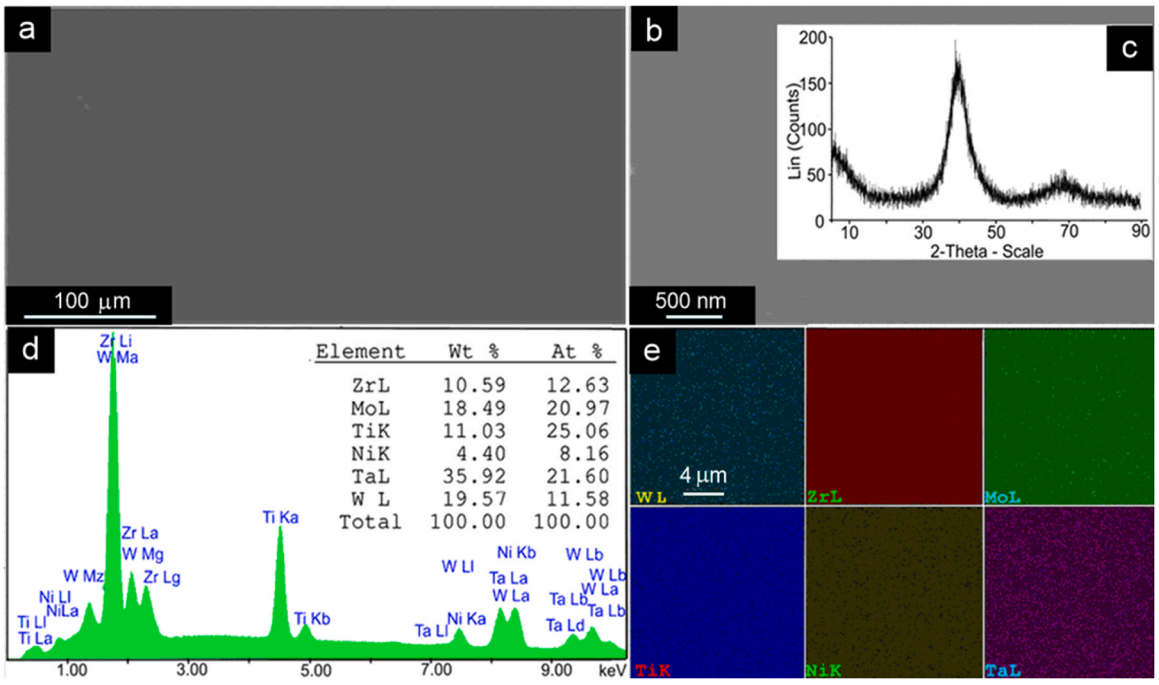

Fig. 6. (a, b) SEM surface morphology investigations at different magnifications; (c) XRD patterns of the layer; (d) SEM-EDX spectrum image; (e) SEM-EDX elemental mapping.

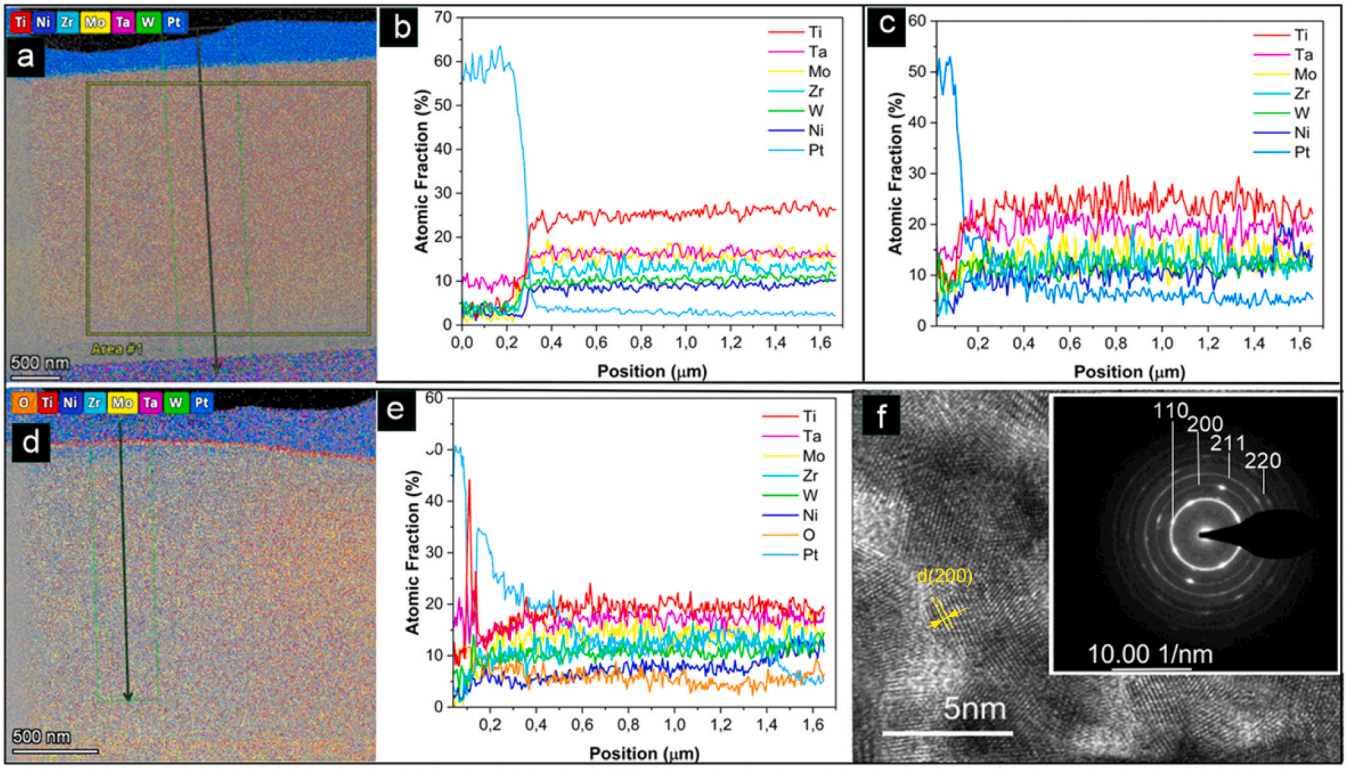

Fig. 7. (a-e) STEM-EDX investigations of the changes of the elemental compositions along the thickness of the films: (a, b) before annealing; (c) after annealing at a temperature of 700°C; (d, e) after annealing at a temperature of 800°C; (f) HR-TEM studies of the microstructure of the layer after annealing at 800°C (insertion: corresponding selected area electron diffraction pattern).

calculated on the basis of the electron diffraction pattern (Fig. 9d) approximately corresponds to the value of 0.102 nm. Bearing in mind the result of the XRD studies (Fig. 9g), it can be said that the nucleation and subsequent growth of the entire array of crystals is governed by the crystal formation along a common growth direction perpendicular to the (310) crystallographic plane that is parallel to the substrate surface.

We also investigated the influence of the elemental composition on the structure formation mechanisms of the patterned layers while

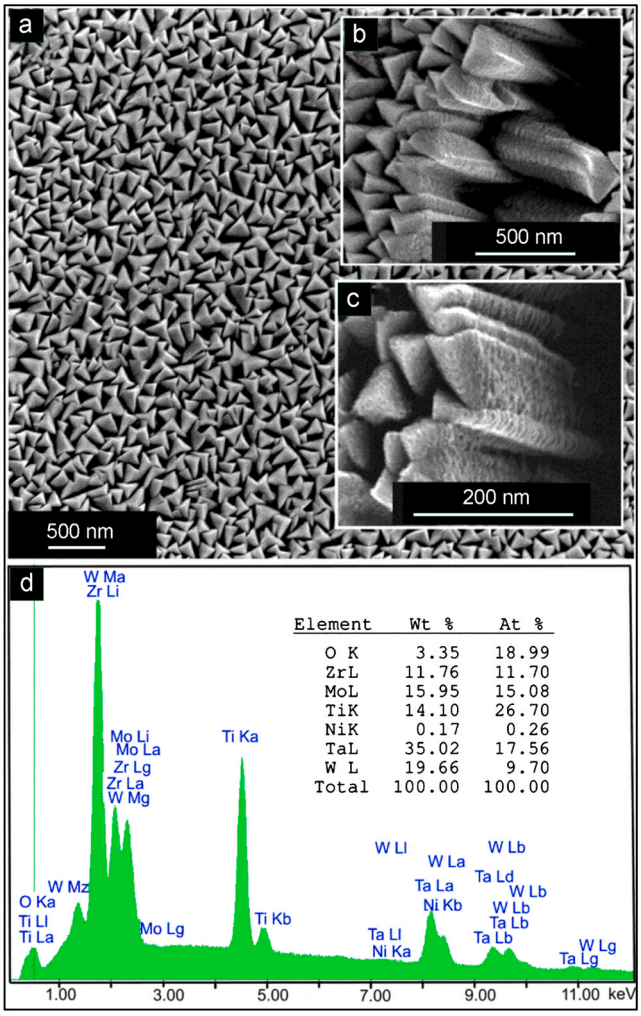

Fig. 8. SEM images of the morphology of the layers (a, b, c) and their corresponding elemental compositions (d).

keeping the Ni concentration constant. It has been established that the change in the concentration of Zr from 10 to 19 at%, Mo from 22 to 35 at %, Ti from 18 to 30 at%, Ta from 15 to 20 at% and W from 13 to 16 at%, has no effect on the structural and morphological characteristics. To conclude, analyzing the entire set of the experimental data, no particular Ni concentration and technological parameter values have been found that correspond to the transition from an amorphous to the crystalline state in ZrTiTaMoWNi thin films. At the same time, a tendency to form crystalline films in the form of patterns at decreasing Ni concentration, together with a reduction of the relative supersaturation of the deposited vapor has been observed.

3.2. *Resistance of Zr–Ti–Ta–Mo–W–Ni layers to the impact of swift heavy Au ions*

From scientific and applied points of view, it is important to establish differences in structural changes under the action of swift heavy ions (SHI) on the amorphous or crystalline layers with approximately the same elemental composition. For this purpose, for the irradiation with Au ions with an energy of 4.8 MeV/u, we used pre-characterized amorphous and crystalline films having the corresponding elemental compositions $Zr_{0.12}Ti_{0.25}Ta_{0.22}Mo_{0.21}W_{0.12}Ni_{0.08}$ and $Zr_{0.15}Ti_{0.3}Ta_{0.21}Mo_{0.18}W_{0.13}Ni_{0.03}$, respectively. In this case, structural changes were studied after irradiating the material with Au SHI at the following fluences: 1×10^{11} ions/cm^2; 2×10^{12} ions/cm^2; 5×10^{12} ions/cm^2; 5×10^{13} ions/cm^2. TEM investigations have shown that irradiation of the amorphous samples with fluences of 1×10^{11} ions/cm^2; 2×10^{12} ions/cm^2; 5×10^{12} ions/cm^2, of 5×10^{13} ions/cm^2 did not cause any changes in the microstructure nor did they cause any crystallization of the samples. In Fig. 10, the results of TEM, SAED, and STEM investigations and STEM EDX elemental mappings are presented for the amorphous sample after irradiation with Au ions with a fluence of 5×10^{13} ions/cm^2. It is observed that the irradiation with a fluence of 5×10^{13} ions/cm^2 has not caused any changes in the structural state of the film (Fig. 10 a,c). Changes of the contrast in the form of vertical lines in the HAADF-STEM image (Fig. 10 c) could be attributed to a FIB curtaining effect that stems from TEM sample preparation. The electron diffraction studies (Fig. 10 b) have not revealed significant changes in the intensity distribution of the electron diffraction patterns. Even after the irradiation with Au ions with the maximum fluence applied in this study, the samples are still amorphous, which evidences the high structural stability and outstanding irradiation resistance of this material. Analyses of the distribution of elements in the amorphous condensate (Fig. 10 d) indicate no signs of segregation after irradiation.

To detect structural changes, SEM studies of the surfaces of the amorphous films (Fig. 11a) were carried out. A careful comparative analysis of the corresponding SEM images of a non-irradiated (Fig. 6a) sample that has a homogeneous surface without any features and the sample irradiated with a fluence of 5×10^{13} ions/cm^2 indicates a higher roughness of the surface layer in the second case, which is the result of the action of Au ions with high energies. Besides that, after irradiation with a fluence of 2×10^{12} ions/cm^2 or higher, swelling is observed to occur in the samples (Fig. 11 b). The step size between regions covered with a mask and irradiated areas of the sample surface measured by laser scanning microscopy (LSM) for a fluence of 2×10^{12} ions/cm^2 was measured as 208 nm. However, taking into account that the samples have a thickness of about 3 μm, the swelling effect could also be explained by volume changes of the substrate material, in this case glass, under the action of high energy Au ions. Besides that, the sputtering of the upper surface layer could lead also to a decrease of the thickness of the deposited material.

The action of Au ions on crystalline layers leads to significant changes of their microstructure. Thus, even at relatively low fluences ($\sim 10^{11}$ ions/cm^2) signs of structural disordering appear in crystalline films, such as the appearance of diffraction maxima in the form of blurred rings in electron diffraction patterns (Fig. 12 a). Upon irradiation of the crystalline films with a fluence of 5×10^{13} ions/cm^2, a transition to a polycrystalline structure occurs with an average crystallite size of ~1–3 nm with structurally disordered boundaries between them (Fig. 12). This conclusion is supported by the blurring and splitting of diffraction maxima in electron diffraction patterns (Fig. 12 e,f), as well as by the fact that the lattice parameter of the bcc lattice after irradiation increased approximately by 0.0007–0.0011 nm. Along with this, pores are formed (Fig. 12b,c) and evolve (Fig. 12d). Based on the fact that the elemental compositions of the amorphous and the crystalline films differ little, the resistance of the condensates to irradiation is mainly determined by their phase state.

Thus, the obtained results indicate a significantly higher resistance of the amorphous phase to irradiation. It is known [19–21] that the relatively high radiation resistance of high-entropy polycrystalline coatings is based on an effective recombination of radiation-induced point defects, primarily at structurally disordered boundaries between crystallites. At the same time, as our studies have shown, the transition from a large-grained polycrystal to a nanostructured coating with disordered grain boundaries under the influence of irradiation was accompanied by the appearance and further growth of radiation-induced pores (Fig. 12 b-d). In this case, the diffusion of point defects into a structurally disordered boundary between several crystallites (Fig. 12) exceeds the capability of the recombination processes. Therefore, it is supposed that there is a critical pore size upon which the recombination has a low probability, so that after exceeding the critical size, further growth

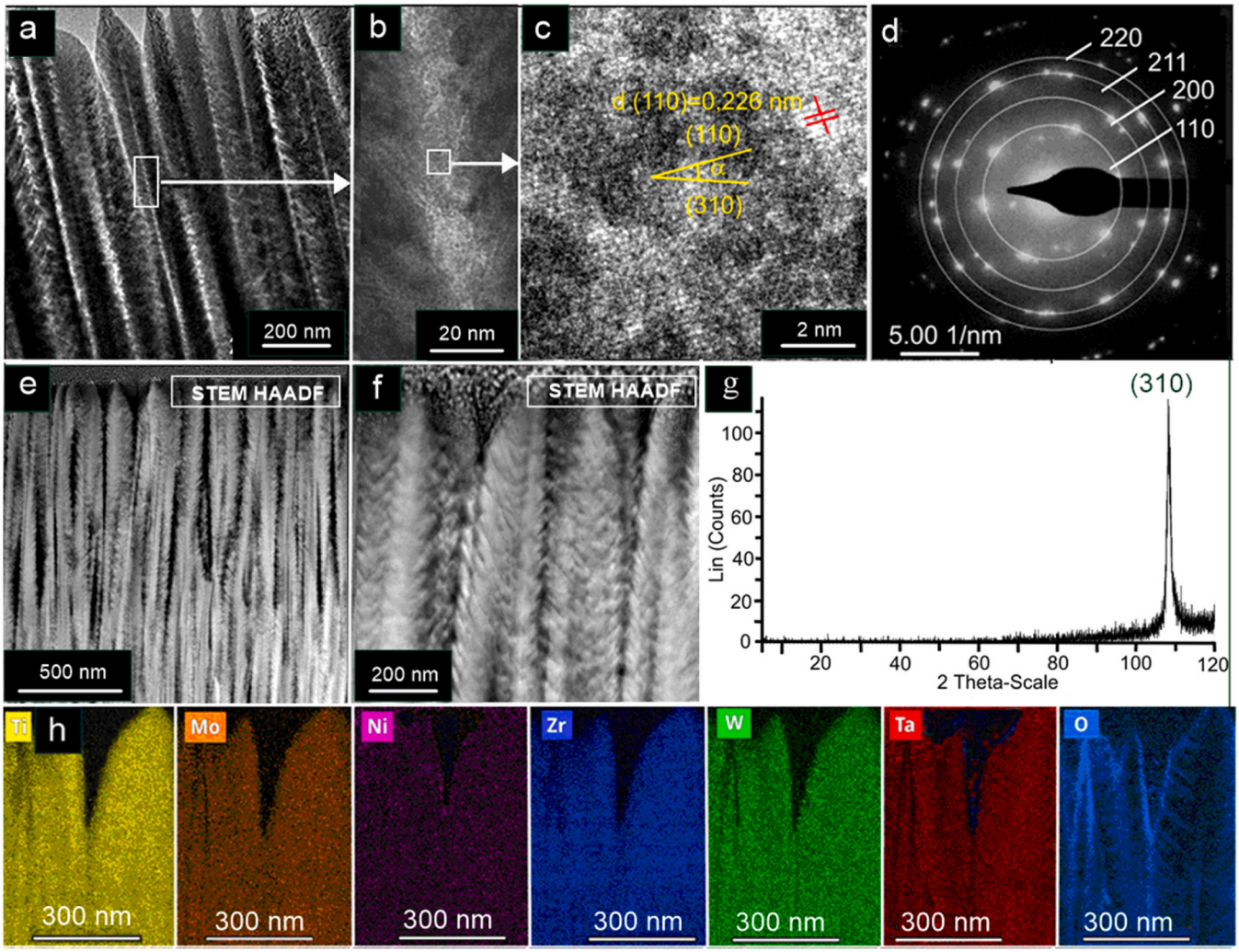

Fig. 9. (a) TEM; (b, c) HR TEM images at different magnifications; (d) SAED; (e, f) HAADF-STEM images at different magnifications; (g) the results of the XRD analysis; (h) STEM-EDX elemental mapping.

occurs via single vacancy attachment (Fig. 12). Thus, the crystalline films are more prone to failure under high-energy Au irradiation, since they lack of an effective mechanism for the relaxation of structural defects, leading to their effective agglomeration and subsequent pore formation.

A comparison of SEM images of the surface morphology of a non-irradiated crystalline film (Fig. 13 a) and a film after irradiation with fluences of 5×10^{12} ions/cm^2 (Fig. 13 b) and 5×10^{13} ions/cm^2 (Fig. 13 c), respectively, evidence an increase of the surface roughness after the irradiation. The observed irradiation-induced nanostructuring and the subsequent increase of the surface-to-volume ratio of the layers could be beneficial for applications of such HEA layers as catalysts, because it is known that the specific surface area plays an important role for the catalytic performance of a given material.

In the amorphous layers, on the contrary, sluggish diffusion hinders the mobility of radiation-induced defects, reducing the likelihood of these defects to form larger pores. Additionally, amorphous materials may exhibit alternative and potentially more effective relaxation mechanisms, such as those associated with the well-known phenomena of “structural relaxation” or “aging”. However, we believe that amorphous layers are not inherently more radiation-resistant. It has been shown in the present work that condensation of multicomponent vapors at relatively high supersaturations results in the formation of amorphous systems that are structurally in a non-equilibrium state. As a result, for such layers even local temperature excursions caused by high-energy ion irradiation could induce significant structural changes at the short-range order level, accompanied by the development of substantial residual stresses that could subsequently cause crack formation (Fig. 5d). In contrast, near-equilibrium condensation in a high-purity inert environment promotes the formation of structurally more relaxed amorphous phase, which exhibits enhanced resistance to the failure mechanisms.

4. Conclusions

It has been demonstrated that using magnetron sputtering from a segmented target in high-purity argon, depending on the condensation temperature, the magnetron discharge power, and Ni concentration, high-entropy Zr–Ti–Ta–Mo–W–Ni layers with different structural and morphological characteristics can be reproducibly formed.

The amorphous films produced under conditions of high relative supersaturation (P_w = 85 W, T_c = 60 °C) exhibit non-equilibrium structural state, as evidenced by significant short-range order rearrangement even at relatively low annealing temperatures (~ 280°C). It has been established that under conditions of low relative supersaturation (P_w = 15 W, T_c = 400°C) and Ni concentrations of approximately 8–15 at%, the formation of structurally stable high-entropy amorphous coatings is favoured. These layers exhibit enhanced elemental intermixing, resulting in a more homogeneous atomic distribution throughout the film. Upon annealing at elevated

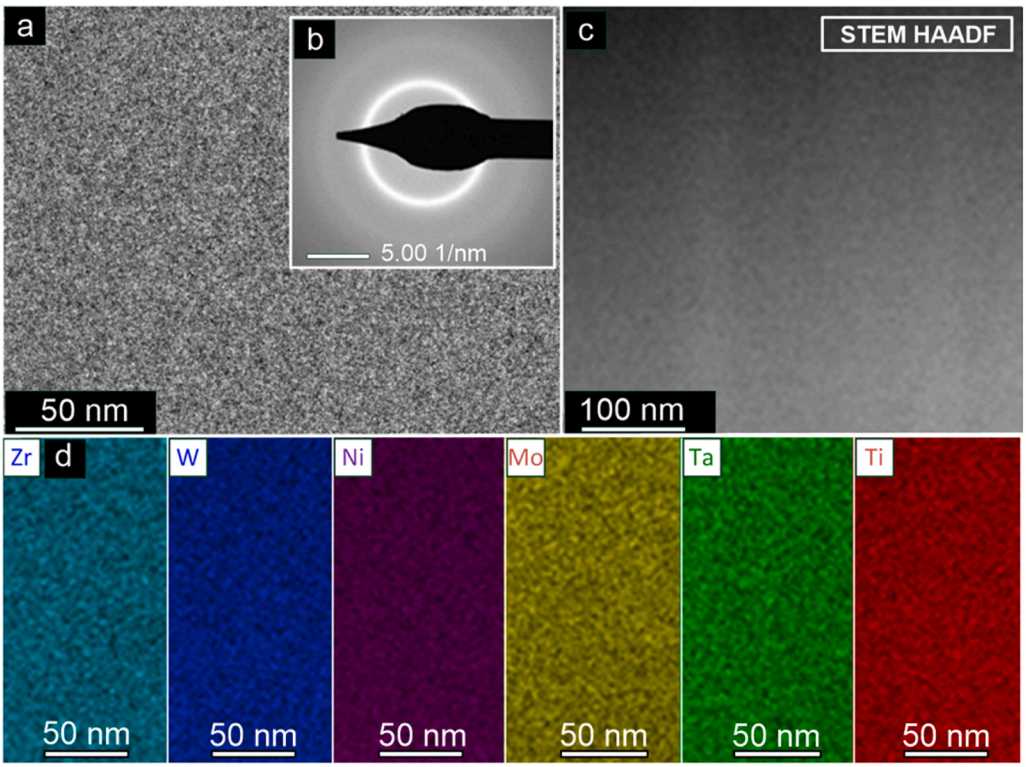

Fig. 10. (a) TEM; (b) SAED; (c) STEM HAADF studies of the structure and (d) STEM EDX elemental compositions in the amorphous layers after their irradiation with Au ions with a fluence of 5×10^{13} ions/cm^2.

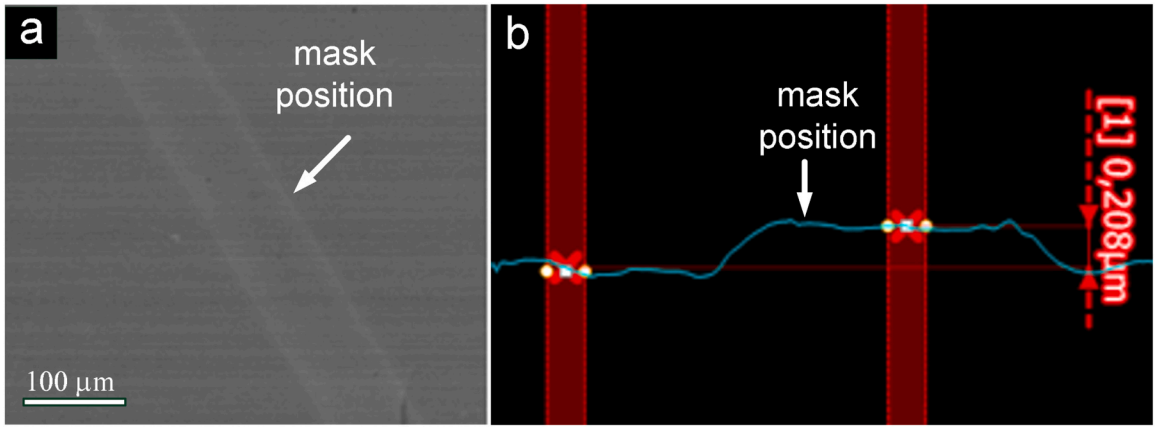

Fig. 11. SEM investigations of the amorphous sample after irradiation(a); LSM measurement of the step height (b).

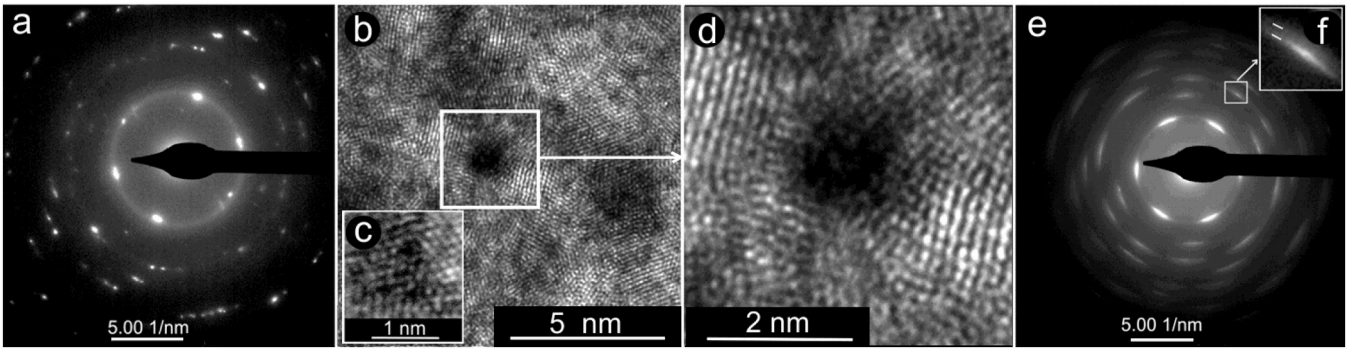

Fig. 12. (a) SAED of a crystalline sample after irradiation with Au ions at a fluence of 10^{11} ions/cm^2 and the corresponding microstructure (b, c, d); (e) SAED pattern and details of the diffraction maximum; (f) detail from (e) at higher magnification after the irradiation of the crystalline layer with a fluence of 5×10^{13} ions/cm^2.

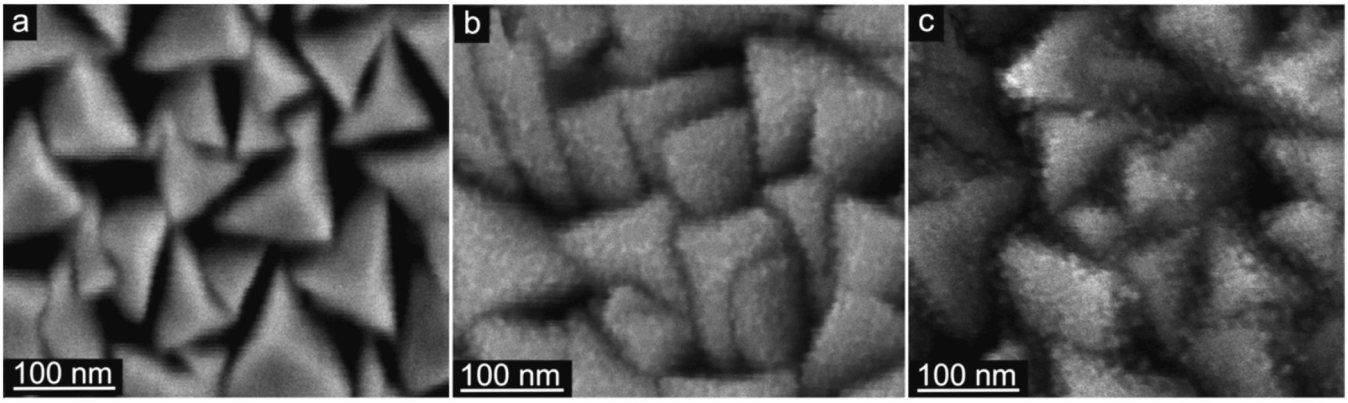

Fig. 13. SEM investigations of the surface morphology of a crystalline layer before (a) and after irradiation with a fluence of (b) 5×10^{12} ions/cm^2 and (c) 5×10^{13} ions/cm^2, respectively.

temperatures (800°C), these films crystallize into a body-centred cubic (bcc) phase.

It was found that a transition to crystalline film formation occurs with decrease in Ni content (down to 3 at%) and simultaneous reduction in the relative supersaturation, achieved by increasing the condensation temperature to 440°C while maintaining $P_w = 15$ W. In this case, the formation of a patterned structure consisting of weakly interconnected columnar bcc crystals oriented along the [310] direction has been observed.

A comparative analysis of the radiation resistance of the obtained amorphous and crystalline high-entropy films under high-energy Au ion irradiation showed that the amorphous phase possesses a significantly higher stability. This advantage of amorphous condensates is attributed to the availability of more efficient defect relaxation mechanisms in the amorphous phase.

CRediT authorship contribution statement

Anna Kornyushchenko: Conceptualization, Investigation, Methodology, Validation, Visualization, Writing – original draft, Writing – review & editing. **Perekrestov Vyacheslav:** Conceptualization, Investigation, Methodology, Project administration, Writing – original draft, Writing – review & editing. **Tomut Marilena:** Conceptualization, Formal analysis, Investigation, Validation. **Dr. Rösner Harald:** Data curation, Formal analysis, Validation, Writing – review & editing. **Peterlechner Martin:** Data curation, Formal analysis, Investigation, Writing – review & editing. **Wilde Gerhard:** Conceptualization, Data curation, Supervision, Writing – review & editing.

Declaration of Competing Interest

The authors declare the following financial interests/personal relationships which may be considered as potential competing interests: Perekrestov Vyacheslav reports financial support was provided by Ministry of Education and Science of Ukraine. Kornyushchenko Anna reports financial support was provided by Philipp Schwartz Initiative of the Alexander von Humboldt Foundation. If there are other authors, they declare that they have no known competing financial interests or personal relationships that could have appeared to influence the work reported in this paper.

Acknowledgement

The work has been performed under support of Ministry of Science and Education of Ukraine, Project Number 0121U112687. Anna Kornyushchenko thanks the Philipp Schwartz Initiative of the Alexander von Humboldt Foundation for supporting her research topic and providing a scholarship that allowed her to continue research work at Institute of Materials Physics, University of Münster, Germany. The Au irradiation results presented here have been performed at the M-branch beamline at the GSI Helmholtz-Zentrum für Schwerionenforschung, Darmstadt (Germany) in the frame of FAIR Phase-0. This work has partially been supported by Deutsche Forschungsgemeinschaft.

References

[1] G.U.O. Sheng, C.T. Liu, Phase stability in high entropy alloys: formation of solid-solution phase or amorphous phase, Progr. Nat. Sci. Mater. Int. 21 (6) (2011) 433–446.
[2] Y. Zhang, Y.J. Zhou, J.P. Lin, G.L. Chen, P.K. Liaw, Solid-solution phase formation rules for multi-component alloys, Adv. Eng. Mater. 10 (6) (2008) 534–538.
[3] H. Luan, K. Li, L. Shi, W. Zhao, H. Bu, P. Gong, K.F. Yao, Recent progress in high-entropy metallic glasses, J. Mater. Sci. Technol. 161 (2023) 50–62.
[4] D.B. Miracle, O.N. Senkov, A critical review of high entropy alloys and related concepts, Acta Mater. 122 (2017) 448–511.
[5] S. Fang, C. Wang, C.L. Li, J.H. Luan, Z.B. Jiao, C.T. Liu, C.H. Hsueh, Microstructures and mechanical properties of CoCrFeMnNiVx high entropy alloy films, J. Alloy. Compd. 820 (2020) 153388.
[6] X. Yu, J. Wang, L. Wang, W. Huang, Fabrication and characterization of CrNbSiTiZr high-entropy alloy films by radio-frequency magnetron sputtering via tuning substrate bias, Surf. Coat. Technol. 412 (2021) 127074.
[7] L.L. Xiao, Z.Q. Zheng, S.W. Guo, P. Huang, F. Wang, Ultra-strong nanostructured CrMnFeCoNi high entropy alloys, Mater. Des. 194 (2020) 108895.
[8] Y. Yue, X. Yan, Y. Zhang, Nano-fiber-structured Cantor alloy films prepared by sputtering, J. Mater. Res. Technol. 21 (2022) 1120–1127.
[9] J. Chen, L. Ren, X. Chen, Q. Wang, C. Chen, J. Fan, S. Shen, Well-Defin. Nanostruct. High. entropy Alloy. Electro Explor. 5 (2) (2025) (April).
[10] A. Obeydavi, A. Shafyei, J.W. Lee, Effect of sputtering power and substrate bias on microstructure, mechanical properties and corrosion behavior of CoCrFeMnNi high entropy alloy thin films deposited by magnetron sputtering method, Intermetallics 172 (2024) 108369.
[11] Z. Wang, C. Wang, Y.L. Zhao, T.H. Huang, C.L. Li, J.J. Kai, C.H. Hsueh, Growth, microstructure and mechanical properties of CoCrFeMnNi high entropy alloy films, Vacuum 179 (2020) 109553.
[12] M. Behera, A. Panigrahi, M. Bönisch, G. Shankar, P.K. Mishra, Structural stability and thermal expansion of TiTaNbMoZr refractory high entropy alloy, J. Alloy. Compd. 892 (2022) 162154.
[13] Xie, P., Yao, Y., Huang, Z., Liu, Z., Zhang, J., Li, T., … & Wang, C.. ,2019. Highly efficient decomposition of ammonia using high-entropy alloy catalysts. Nature communications, 10(1), 4011.
[14] L. Ju, W. Wu, Y. Zhou, Y. Zhang, Q. Wang, Electrodeposition of FeNiCoCrMn high-entropy alloys on copper foam for enhanced hydrogen evolution reaction - influence of additives and deposition potential, Mater. Lett. 374 (2024) 137195.
[15] Gao, W., Feng, M., Chen, C., & Lian, G. ,2025. Microstructure evolution, wear resistance and corrosion resistance of CoCrCu0. 5FeNiSix high-entropy alloy coatings fabricated by laser cladding. Journal of Materials Research and Technology.
[16] Lou, B.S., Li, C.L., Annalakshmi, M., Hung, T.Y., & Lee, J.W. ,2025. Exploring the effect of Ti and Al contents on the microstructural, mechanical, and corrosion resistance features of VNbMoTaWTiAlN refractory high entropy alloy coatings. Materials Chemistry and Physics, 130901.
[17] H. Yu, W. Liang, Q. Miao, M. Yin, Y. Xu, J. Gao, S. Sun, High-temperature oxidation resistance and wear properties of functionally graded CrHfNbTaTiN high-entropy nitride coating on Ti alloy, Appl. Surf. Sci. 680 (2025) 161474.

[18] T. Xu, J. Li, Y. Yu, T. Li, L. Wang, H. Tang, Z. Qiao, High-temperature tribological properties of $Fe_{50}Mn_{25}Cr_5Al1_5Ti_5$ iron-based high-entropy alloys, Tribology Int. 204 (2025) 110423.
[19] E.J. Pickering, A.W. Carruthers, P.J. Barron, S.C. Middleburgh, D.E. Armstrong, A. S. Gandy, High-entropy alloys for advanced nuclear applications, Entropy 23 (1) (2021) 98.
[20] Du, X., Pu, G., Li, J., Zhang, K., Yang, J., Liu, P., … & Liu, B. ,2024. Microstructural evolution and radiation resistance of amorphous TiTaNbZr multi-principal elements alloy induced by Au ion irradiation at elevated temperatures. Journal of Alloys and Compounds, 1008, 176444.
[21] Z. Cheng, J. Sun, X. Gao, Y. Wang, J. Cui, T. Wang, H. Chang, Irradiation effects in high-entropy alloys and their applications, J. Alloy. Compd. 930 (2023) 166768.
[22] V. Perekrestov, A. Kornyushchenko, Y. Kosminska, M. Kubakh, G. Wilde, Self-organization of micro-and nanosystems in the form of patterns, Crystals 14 (11) (2024) 953.
[23] Korniushchenko, A.S., Kosminska, Y.O., Shevchenko, S.T., Natalich, V.V., & Perekrestov, V.I. ,2021. Stages of Cr, Zn, Cu, Si, Ag, and Al Nucleation under Quasi-equilibrium Condensates of Ion-sputtered Atoms.
[24] A. Kornyushchenko, Y. Kosminska, S. Shevchenko, G. Wilde, V. Perekrestov, Structural, morphological and sensor properties of the fractal-percolation nanosystem ZnO/NiO, J. Electron. Mater. 50 (2021) 2268–2276.
[25] V.I. Perekrestov, A.I. Olemskoi, Y.O. Kosminska, A.A. Mokrenko, Self-organization of quasi-equilibrium steady-state condensation in accumulative ion-plasma devices, Phys. Lett. A 373 (37) (2009) 3386–3391.
[26] Alvi, S., Milczarek, M., Jarzabek, D.M., Hedman, D., Kohan, M.G., Levintant-Zayonts, N., … & Akhtar, F. ,2022. Enhanced mechanical, thermal and electrical properties of high-entropy HfMoNbTaTiVWZr thin film metallic glass and its nitrides. Advanced Engineering Materials, 24(9), 2101626.
[27] C. Gammer, C. Mangler, C. Rentenberger, H.P. Karnthaler, Quantitative local profile analysis of nanomaterials by electron diffraction, Scr. Mater. 63 (3) (2010) 312–315.